



Structural, Optical and Magnetic Properties of $\text{Zn}_{1-x}\text{Cd}_x\text{O}$ Diluted Magnetic Semiconductors Nanoparticles

M. Yehia¹ · Sh. Labib² · S. M. Ismail¹

Received: 30 April 2021 / Accepted: 4 June 2021 / Published online: 20 June 2021
© The Author(s), under exclusive licence to Springer Science+Business Media, LLC, part of Springer Nature 2021

Abstract

$\text{Zn}_{1-x}\text{Cd}_x\text{O}$ ($x=0, 0.001, 0.01, 0.1$) nanoparticles were prepared using polyol technique. The prepared nanoparticles were characterized using X-ray diffraction (XRD), Fourier transformed infrared (FTIR) spectroscopy, scanning electron microscope (SEM), high resolution transmission electron microscope (HRTEM), ultraviolet–visible absorbance spectroscopy (Uv–Vis), vibrating sample magnetometer (VSM) and electron spin resonance (ESR). XRD confirmed the purity of the prepared samples, where all the samples crystallized in single hexagonal wurtzite phase. The morphology of the nanoparticles is studied using SEM and HRTEM techniques. The Uv–vis studies showed a marked red shift in the energy gap values of the prepared samples with respect to the theoretical value. VSM measurements suggested that only $\text{Zn}_{0.09}\text{Cd}_{0.01}\text{O}$ exhibit room temperature ferromagnetism, whereas, the other samples show diamagnetic behavior. ESR measurements spotlights on the presence of different types of defects in the prepared samples.

Keywords Diluted magnetic semiconductors · $\text{Zn}_{1-x}\text{Cd}_x\text{O}$ · Optical properties · Bound magnetic polaron · Electron spin resonance

1 Introduction

Zinc oxide (ZnO) attracts the attention due to its promising properties that allow it to be used in varieties of potential applications as: room-temperature ferromagnetic, magneto-optic, photocatalytic, antibacterial, piezoelectric, chemical-sensing, doping-depended electrically conductive properties, photovoltaic cells, an emitter layer and antireflection (AR) coating, the fabrication of potentially high efficiency and low-cost solar cells [1–3]. Consequently, ZnO has wide range of catalytic, electrical, optoelectronic, and photochemical properties [4–7].

ZnO is considered as an active optical component due to its potential use as a replacement of GaN for UV light emission devices, light-emitting diodes, nanolasers,

photo-detectors, and nanosensors [8]. The way is open to ZnO to be used in the semiconductor industry and in optoelectronic devices due to its abundance and being environmentally friendly and its properties as the wide band-gap (~3.37 eV) with a large exciton binding energy (~60 meV) and biexciton binding energies (on the order of 25 meV thermal energy) at room temperature making it attractive for low-cost and high-efficiency LEDs and lasers near the UV band, and it is more abundant in natural resources [2, 8–10].

A successful approach to decrease the band gap is doping ZnO with transition metals (TM), which expands the spectral response to the visible region and leads to improve the photocatalytic activity of ZnO [11, 12]. In the same time, ZnO is one of the diluted magnetic semiconductors (DMSs) obtained by doping ZnO with a small amount of TM ions [13]. Especially it is known that diluted magnetic semiconductors (DMS) are materials in which transition metals or rare earth ions are doped in the crystalline lattice, giving rise to ferromagnetic properties in the doped semiconductor [14]. Since the most used semiconductors do not have suitable magnetic properties, it is necessary to introduce the ferromagnetism. The main way to obtain ferromagnetic semiconductors is doping with transition metal (TM) ions (Fe, Cr, V, Ni, Mn) in semiconducting hosts, such as TiO_2 , ZnS,

✉ M. Yehia
m6yehia@yahoo.com

¹ Reactor Physics Department, Nuclear Research Center, Egyptian Atomic Energy Authority, P. O. Box 13759, Cairo, Egypt

² Nuclear Chemistry Department, Hot Laboratories Center, Egyptian Atomic Energy Authority, P. O. Box 13759, Cairo, Egypt

and ZnO [14]. Subsequently, there are several reports that claimed room temperature ferromagnetism (RTFM) in Mn, Co, Ni and Fe doped ZnO. However, the origin and exchange mechanism responsible for RTFM in these materials are still controversial [15]. Today there is a consensus that the TM doping is not a sufficient condition to achieve the RTFM, and those point defects in the structure of such materials play an important role to reach the desired magnetic properties [15]. From this point we have chosen a non-magnetic doping to ZnO and studied its RTFM behavior.

To make this study it is important to choose a suitable preparation method to control the achieved properties of the prepared materials. So by controlling the particle sizes using suitable preparation methods, the band gap and magnetic properties can be engineered [16]. Especially it is known that both doping and different preparation conditions yields to various amount and types of vacancies in these materials, which strongly affect the electrical, magnetic, and optical properties of ZnO. The hexagonal ZnO and cubic CdO have very different crystal structure, and also, low thermodynamic solubility, which make it difficult to obtain single phase ZnO doped with high Cd content [17].

In the present work, $Zn_{1-x}Cd_xO$ nanoparticles were successfully prepared in a single hexagonal wurtzite phase using a simple polyol method that has the advantage of simplicity, purity, high yield, and low cost [18]. The structural, morphological and optical properties were studied using X-ray powder diffraction (XRD), Fourier transformed infrared spectroscopy (FTIR), scanning electron microscope (SEM), high resolution transmission electron microscope (HRTEM) and ultraviolet visible (UV–vis) spectroscopy measurements. The change of the band gap energy with increasing cadmium content was identified from UV–vis spectroscopy. The magnetic properties were investigated using vibrating sample magnetometer (VSM) and electron spin resonance (ESR).

2 Experimental

2.1 Materials and Methods

Nano $Zn_{1-x}Cd_xO$ ($x=0, 0.001, 0.01$ and 0.1) powders were prepared using zinc nitrate hexahydrate ($Zn(NO_3)_2 \cdot 6H_2O$, 99% Merck, Germany); cadmium nitrate tetrahydrate ($Cd(NO_3)_2 \cdot 4H_2O$, 99% Merck, Germany); glycerol ($C_3H_8O_3$, 99.5% Genchem, China). The solutions were prepared using deionized water from a Millipore water purification system and having a resistivity of $18.2 M\Omega$.

Different prepared samples were prepared using a simple green route (polyol auto combustion method) that is derived from (the sol–gel–auto combustion) method given in [18]. ZnO was prepared by dissolving $Zn(NO_3)_2 \cdot 6H_2O$ in an appropriate amount of glycerol and 20 ml distilled water.

While the doped samples in $Zn_{1-x}Cd_xO$ ($x=0.001, 0.001$ and 0.1) were prepared by dissolving the stoichiometric ratio of $Zn(NO_3)_2 \cdot 6H_2O$ and $Cd(NO_3)_2 \cdot 6H_2O$ in the appropriate amount of glycerol/distilled water as in the same case of pure ZnO. Viscous gels are formed, and the complete dissolution of the added precursors was achieved by stirring on a hot plate at $100\text{ }^\circ\text{C}$. The dissolved gels were kept on the hot plate until a strong explosion of the different samples occurred and very fine powders were obtained. The obtained powders were calcined at $300\text{ }^\circ\text{C}/4\text{ h}$ using a heating rate of $10\text{ }^\circ\text{C}/\text{min}$ and thermally treated at $500\text{ }^\circ\text{C}/4\text{ h}$ using the same used heating rate. Finally the thermally treated powders were ground for 30 min. A schematic diagram of different $Zn_xCd_{1-x}O$ step formation is shown in Fig. 1. The chemical structure was started by a complexation between the hydrolyzed salts in the glycerol solution and glycerol to form metal glycerolate complex (when the sol is kept on the hot plate). The complex of glycerolate breaks down to $Zn_{1-x}Cd_xO$ under the effect of thermal treatment. Very fine powders are obtained after grinding using pestle and mortar.

2.2 Characterization

The structure of the prepared samples was studied at room temperature using x-ray diffraction (XRD) analysis (Philips X'Pert multipurpose diffractometer) with $CuK\alpha$ radiation (with $\lambda=1.5418\text{ \AA}$). The crystal structure was refined by the Rietveld profile method using Rex software [19]. Fourier-transform infrared (FTIR) spectroscopy (Nicolet iS10 FTIR Spectrometer; Thermo Scientific) was carried out on the prepared powders using the KBr disc technique, scanning was carried out in the region of 400 to 2000 cm^{-1} . Microstructural investigations of the different powders were carried out using: scanning electron microscope (SEM, JSM-6510 LA; JEOL, Japan) in high vacuum mode using an accelerating voltage of 30 kV , working distance of 12 mm , and magnification of $X 5000$ and high resolution transmission electron microscope (HRTEM JEOL 2100, Japan) using an

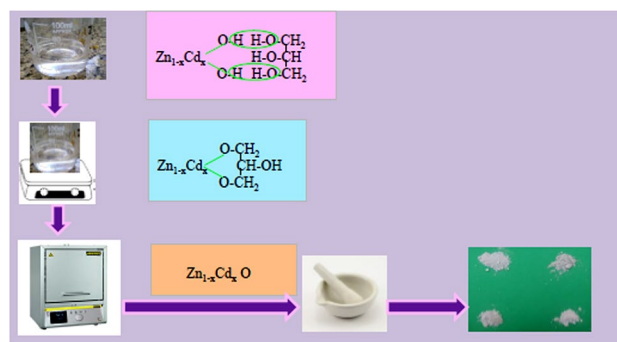


Fig. 1 Schematic diagram showing the different $Zn_xCd_{1-x}O$ step formation up to get fine powders

accelerating voltage of 200 kV and magnification \times (25,000, 30,000 and 40,000). Prior to the analysis the prepared samples were dispersed in distilled water and ultrasonicated for 30 min using (Ultrasonic Branson 1510). Optical studies were performed using ultraviolet–visible (UV–Vis) absorbance spectroscopy (6850 UV–Vis spectrophotometer Jenway), using distilled water/conc HNO_3 solution as reference, with the analysis at different wavelengths ranging from 360 to 1100 nm. Magnetic measurements on the synthesized nanoparticles were carried out using vibrating sample magnetometry (VSM, 9600-1 LDJ, USA) with a maximum applied field of nearly 20 kG at room temperature to determine the saturation magnetization M_s and coercivity H_c . Electron spin resonance (ESR) measurements were carried out at frequency of $\nu = 9.71$ GHz using a standard X-band Bruker EMX spectrometer.

3 Results and Discussion

3.1 X-Ray Diffraction Analysis Measurements (XRD)

Figure 2 shows the XRD diffraction patterns of $\text{Zn}_{1-x}\text{Cd}_x\text{O}$ nanoparticles. All the samples show a hexagonal wurtzite structure with space group $P6_3mc$ no. 186. Using the Rex software, the lattice parameters (a and c) and the average

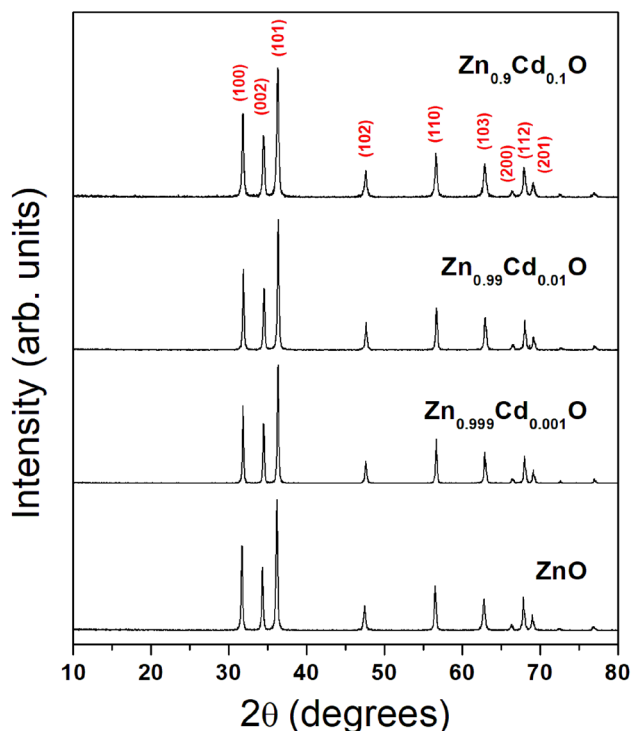


Fig. 2 XRD patterns of $\text{Zn}_{1-x}\text{Cd}_x\text{O}$ nanoparticles with different Cd concentrations

particle size D were determined (Table 1). As illustrated in Fig. 3, the lattice parameters show weak dependence on x . Both a and c increase slightly by increasing the Cd content (x). This increase of the lattice parameters is accompanied with a decrease of the c/a ratio. In general, the values of a , c and c/a are within the expected values of single hexagonal phase of ZnO [20]. The ionic radius of Zn^{2+} and Cd^{2+} ions are 0.60 Å and 0.78 Å, respectively [21]. Hence, the increase of a and c can be attributed to the differences in the ionic radius of the two ions. The particle size of different $\text{Zn}_{1-x}\text{Cd}_x\text{O}$ nanoparticles is presented in Fig. 4 and Table 1. For pure ZnO, the average particle size is amount to 72 nm. D increases significantly with the initial doping with Cd and reaches 111 nm. For $x = 0.01$ and 0.1, D decreases continuously to 46 and 28 nm, respectively.

In general, XRD peak broadening β is attributed to the crystallite size and lattice strain, and therefore is expressed as [22]:

Table 1 The lattice parameters a , c and the ratio c/a for different $\text{Zn}_{1-x}\text{Cd}_x\text{O}$ nanoparticles

x	a (Å)	c (Å)	c/a
0	3.284	5.263	1.6025
0.001	3.286	5.265	1.60227
0.01	3.291	5.273	1.60214
0.1	3.295	5.279	1.60198

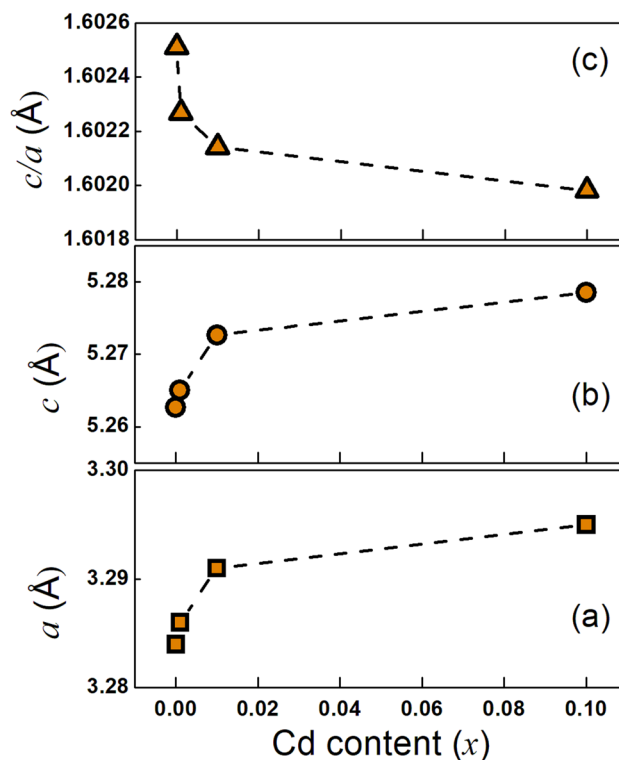


Fig. 3 **a** The lattice parameter a , **b** The lattice parameter c and **c** The ratio c/a for different $\text{Zn}_{1-x}\text{Cd}_x\text{O}$ nanoparticles

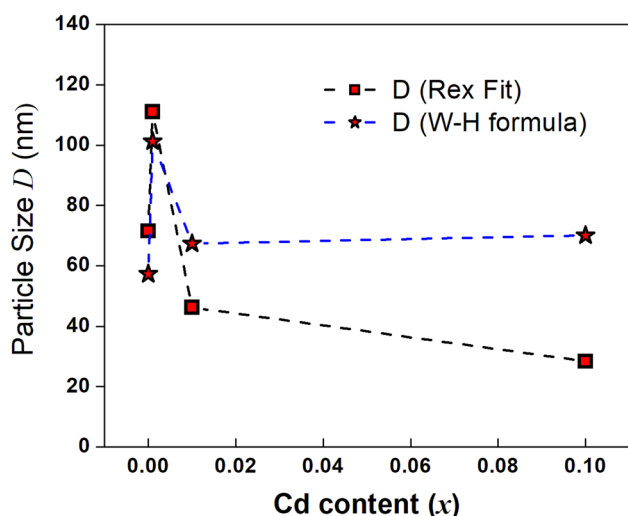


Fig. 4 The particle size D calculated from the Rex fit and W–H plots of different $\text{Zn}_{1-x}\text{Cd}_x\text{O}$ nanoparticles

$$\beta = \frac{\lambda k}{D \cos\theta} + 4\varepsilon \tan\theta \quad (1)$$

where λ is the XRD wavelength (CuK_α radiation with $\lambda = 1.5418$), $k = 0.9$, D particle size and ε microstrain. The Williamson and Hall plot can be obtained from:

$$\beta \cos\theta = \frac{\lambda k}{D} + 4\varepsilon \sin\theta \quad (2)$$

The relation between $\beta \cos\theta$ and $\sin\theta$ for different $\text{Zn}_{1-x}\text{Cd}_x\text{O}$ nanoparticles is illustrated in Fig. 5. From the linear fit of these graphs, the microstrain can be calculated out of the slope and the particle size is obtained from the interception of the line with y-axis ($\beta \cos\theta$). The microstrain is shown in Fig. 6a, whereas, ε increased for all the doped samples. Interestingly, the particle size calculated from the W–H plot shows the same behavior of the particle size calculated from the Rietveld method using the Rex software. In this case, for ZnO , $D = 57$ nm and by initial doping with Cd it increases to $D = 101$ nm and then decreases for further increases of $x = 0.01$ and 0.01 to $D = 67$ and 70 nm, respectively.

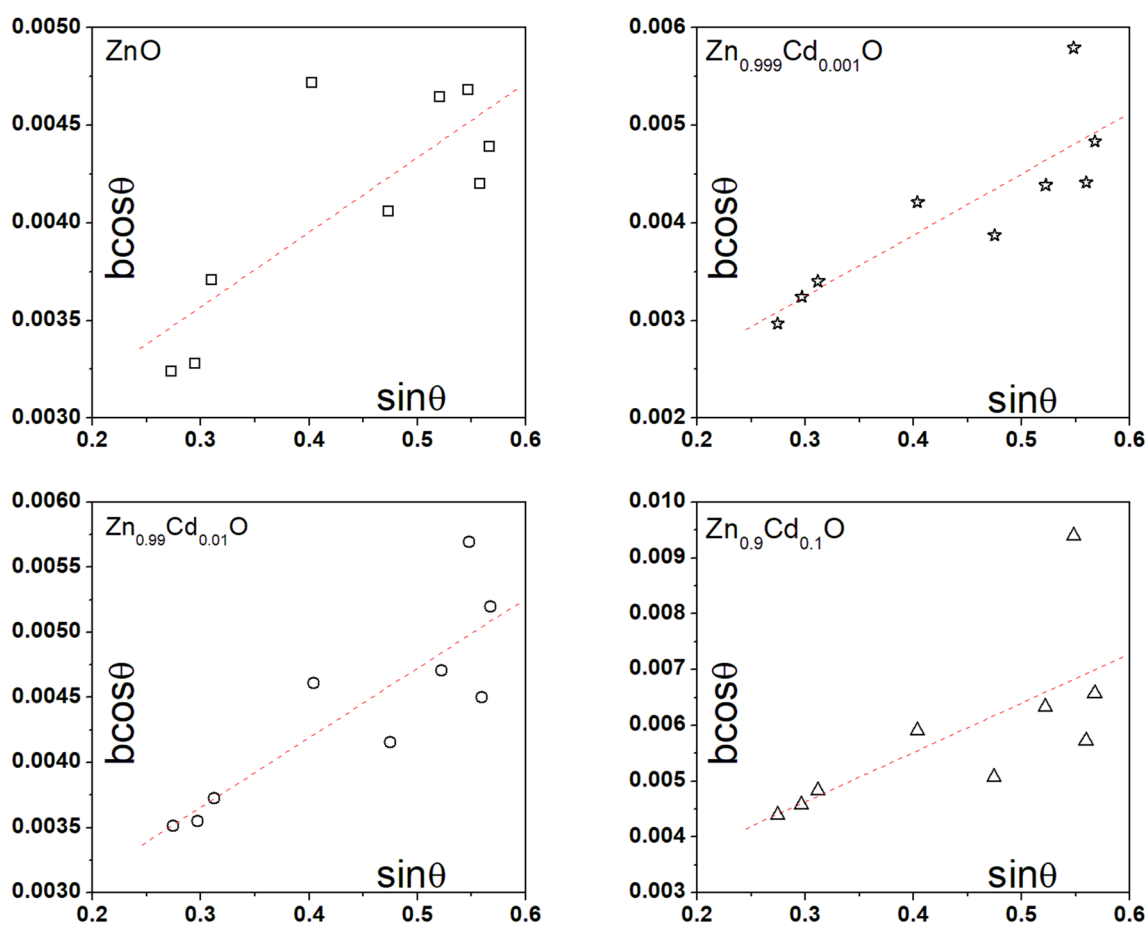


Fig. 5 W–H plots of different $\text{Zn}_{1-x}\text{Cd}_x\text{O}$ nanoparticles

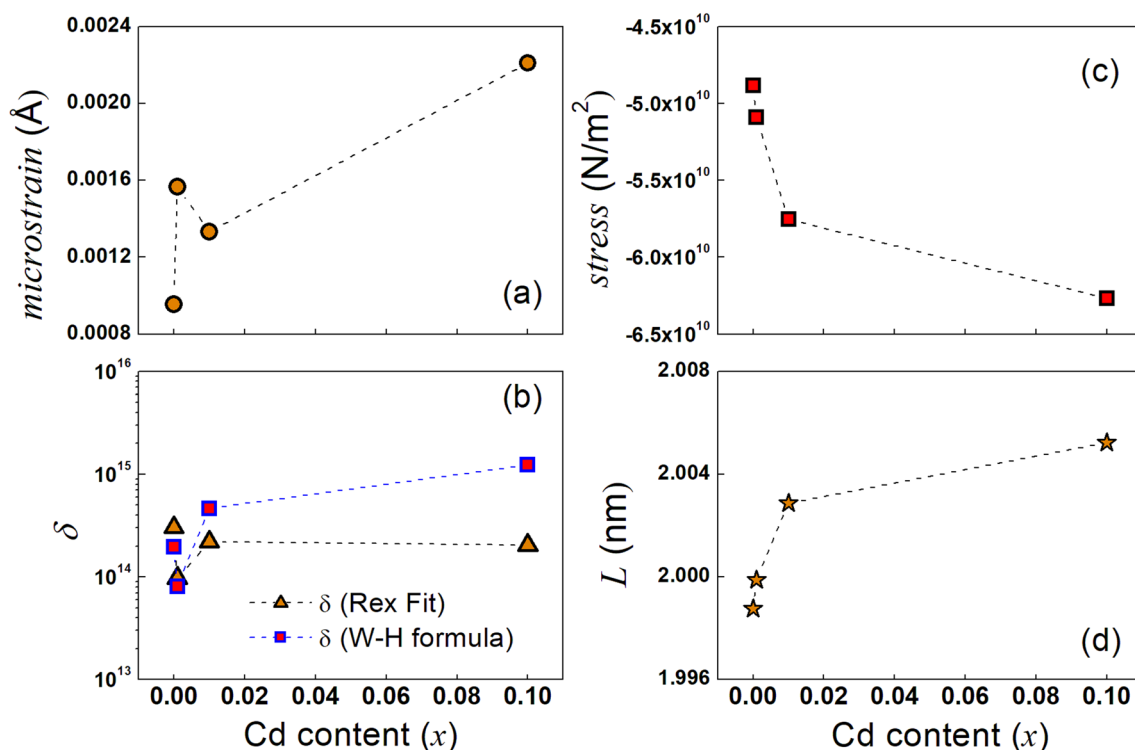


Fig. 6 **a** Microstrain ϵ , **b** Dislocation density values (δ), **c** Stress, **d** The bond length L of different $\text{Zn}_{1-x}\text{Cd}_x\text{O}$ nanoparticles

The stress (σ) was calculated using the relation:

$$\sigma = -453.6 \times \left(\frac{c - c_0}{c_0} \right) \times 10^9 \quad (3)$$

where, c_0 is the lattice constant in the unstrained ZnO. The stress decreases gradually by introducing Cd^{2+} ions to ZnO unit cell. The negative sign of the values corresponds to compressive stress values. The dislocation density (δ) was obtained as:

$$\delta = \frac{1}{D^2} \quad (4)$$

Figure 6b shows the values of δ calculated from the particle size obtained from both Maud fitting and W–H plot. The obtained low δ values are indication of a good crystallinity in $\text{Zn}_{1-x}\text{Cd}_x\text{O}$ nanoparticles. The displacement of an atom from its lattice site u can be calculated as:

$$u = \left(\frac{a^2}{3c^2} \right) + \frac{1}{4} \quad (5)$$

In this case, the bond length L of $\text{Zn}_{1-x}\text{Cd}_x\text{O}$ nanoparticles was calculated by:

$$L = \sqrt{\left(\frac{a^2}{3} \right) + (0.5 - u)^2 c^2} \quad (6)$$

The values of u are almost constant as illustrated in Table 2, whereas, the bond length L values are increasing gradually by introducing Cd content. Logically, this increase is related to the replacement of Zn^{2+} ions with Cd^{2+} ions which are characterized by bigger ionic radius.

Table 2 The particle size (D) calculated from W–H plot, microstrain (ϵ), the stress (σ), dislocation density (δ), displacement (u) and bond length (L) for different $\text{Zn}_{1-x}\text{Cd}_x\text{O}$ nanoparticles

x	D (W–H) (nm)	D (Rex) (nm)	ϵ (Å)	σ $\text{N/m}^2 (10^{10})$	δ (Rex) $\text{m}^{-2}(10^{14})$	δ (W–H) $\text{m}^{-2}(10^{14})$	u	L (nm)
0	57	72	0.000955	– 4.883	3.042E14	1.953E14	0.3798	1.9988
0.001	101	111	0.00157	– 5.093	9.750E13	8.109E13	0.37984	1.9999
0.01	67	46	0.00133	– 5.755	2.205E14	4.667E14	0.37986	2.0029
0.1	70	28	0.00221	– 6.267	2.037E14	1.237E15	0.37989	2.0052

3.2 Fourier Transform Infrared Spectroscopy

FTIR spectra evolution of the prepared powders is shown in Fig. 7. The analysis focuses on the region from 2000 to 400 cm^{-1} . The present peak at 1729 cm^{-1} is attributed to carbonyl (C=O) group [23]. This group appearance is referred to the soaps, unreacted fats and oils as non-glycerol organic materials that are present in glycerol [24]. As known these materials are characterized by the presence of carboxylic group. The peak at 1378 cm^{-1} corresponds to the bending vibration of C–H [23] due to the use of glycerol in the preparation method. The small peaks at 1508, 1470, 1384 cm^{-1} are due to C–H bending vibrations present in glycerol [23, 25]. C–O stretching vibrations are also found at 1180 cm^{-1} [23, 25]. The characteristic stretching vibration of Zn–O bond is observed at 426 cm^{-1} , Fig. 7. The shift in the vibration mode of Zn–O in the doped samples to 433, 430 and 428 cm^{-1} , respectively as shown in Fig. 7, is due to the stress acting on ZnO nanoparticles when incorporating Cd^{2+} ions in crystal lattice of Zn–O [26]. The increase in the intensity of Zn–O peak is related to the increase in the number of Zn–O bonds [27]. The high broadness observed in Zn–O peaks is related to the intense number of the defect present in the samples as confirmed from ESR measurements.

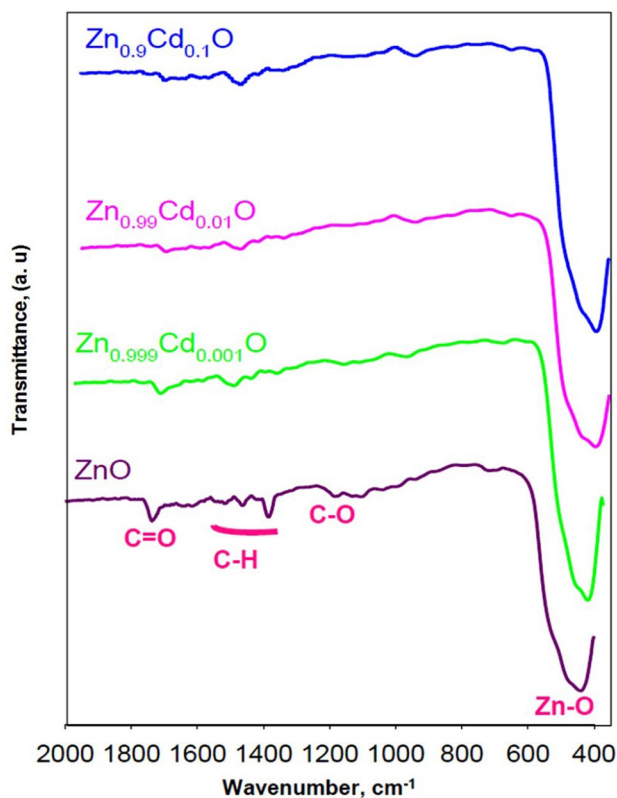


Fig. 7 FTIR measurements of different $\text{Zn}_{1-x}\text{Cd}_x\text{O}$ nanoparticles

3.3 Scanning Electron Microscope (SEM)

Figure 8 shows the SEM images of the $\text{Zn}_{1-x}\text{Cd}_x\text{O}$ thermally treated at 500 $^\circ\text{C}$ /4 h. As shown in these figures, very fine structure of tinny crystallites of few nm is obtained and no marked variation in the microstructure is observed with the addition of Cd^{2+} ions. The images revealed the uniform distribution of the present particles [28].

3.4 High Resolution Transmission Electron Microscope (HRTEM)

A detailed investigation of the morphological properties of the prepared materials is studied using HRTEM and given in Fig. 9. $\text{Zn}_{1-x}\text{Cd}_x\text{O}$ consisted of nanoparticle with different shapes. Regular and irregular hexagonal, cylindrical nanoparticles and nanocubes, having a diameter in the range of (37–80) nm, are observed, Fig. 9. The increase of Cd doping percent shows a decrease in the regular hexagonal shape nanoparticles with respect to the other shapes. The sample $\text{Zn}_{0.999}\text{Cd}_{0.001}\text{O}$ shows a marked increase in the particle size with respect to ZnO. Further increase in the doping percent show lower particle size values. The present nanoparticles show coalescence along the surface planes having easy directions with a lower surface free energy [29]. Wurtzite ZnO has two polar planes [0001] and [000 $\bar{1}$] and two non-polar planes [1010] and [110] [29]. Under normal conditions the non-polar planes are exposed due to their lower surface free energies [29]. With increasing the doping of Cd^{2+} ions, the surface energies of the polar planes is decreased due to the electrostatic interactions between positive and negative ions in the solution [29]. Consequently different shapes are formed and the degree of coalescence between the different particles, which are exposed with polar planes, increased in the doped samples.

3.5 Ultraviolet–Visible Absorbance Spectroscopy (Uv–Vis)

The Uv–vis absorption spectra of ZnO thermally treated at 500 $^\circ\text{C}$ for 4 h are shown in Fig. 10a. The absorption edge is observed at (450–490) nm. From the given curve; it is observed that the prepared powders have high absorption in the visible region up to 1100 nm.

The energy gap is determined from Tauc's plot using the relation:

$$\alpha h\nu = A(h\nu - E_g)^{n/2} \quad (7)$$

where α is the absorption coefficient, h is Planck constant, ν is incident light frequency, E_g is band gap energy, and A is a

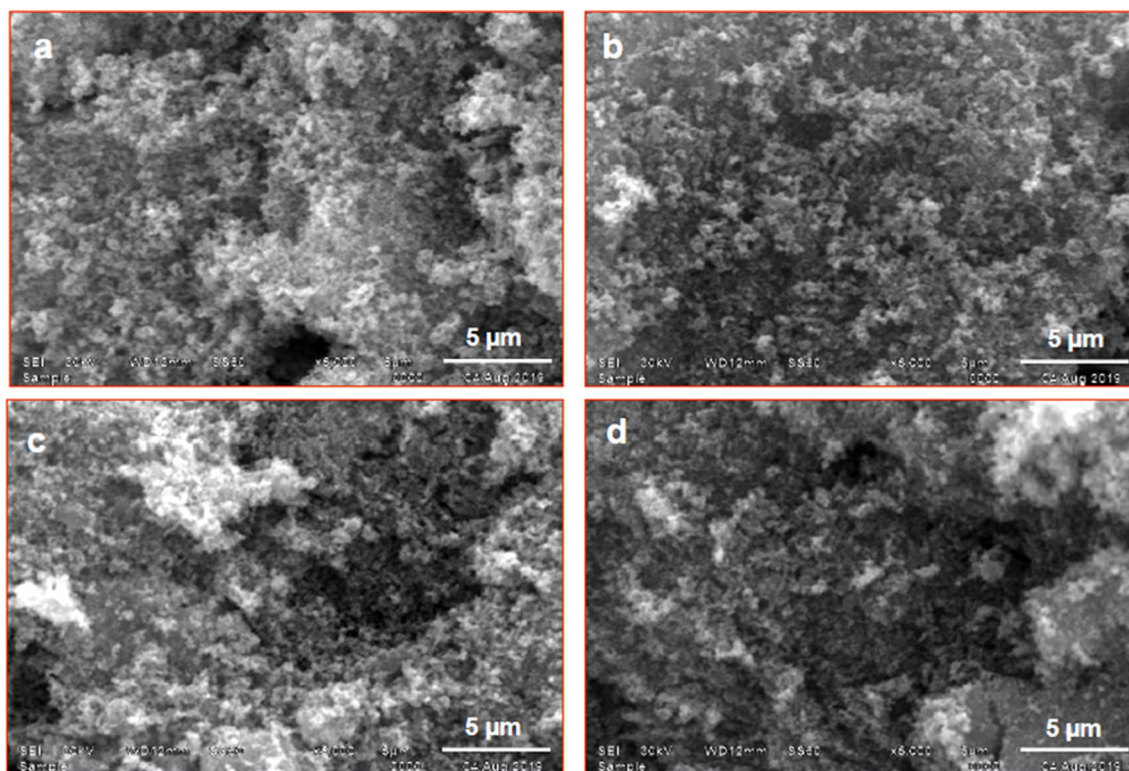


Fig. 8 SEM images of different $Zn_{1-x}Cd_xO$ nanoparticles

constant. The value of n is dependent on the type of transition in the optical semiconductor [18, 30].

A red shift in the energy gap (2.75 eV) of the prepared ZnO powder is obtained with respect to the theoretical value (3.33–3.37) eV of the bulk ZnO as given from literature [31], Fig. 10b. Both extrinsic and intrinsic factors are the key parameters of the marked observed red shift in the energy gap of the prepared ZnO.

Extrinsic factors are reflected from the high reactivity of the used preparation method leading to the formation of highly defective materials where new defects are introduced into the prepared ZnO through the preparation method. So the preparation method gives us a new observation for understanding the properties of the studied materials. The high explosion produced through the preparation method involves the transport of thermal vibration at the interfaces as thermal waves [32]. The resulting wave interference leads to the formation of forbidden band gap which are common in semiconductor materials [32]. The propagation of these thermal waves into the studied materials leads to the formation of thermal phonons that reflect the reason of why pure ZnO has a lower energy gap than that given in literature. The produced phonons react with the other defects in ZnO that is enriched by large number of defects at the grain boundary regions.

The different phonons produced have properties as: phonon dispersion, group velocities, phonon relaxation times and phonon scattering phase space that affect the thermal conductivity as well as the energy gap of the ZnO [33].

Intrinsic factors are related to the type of different defects present in ZnO. Where, the origin of visible absorption is due to the different type of defects present in ZnO [21]. The known defects are: zinc interstitial (Zn_i), zinc vacancy (V_{Zn}), oxygen interstitial (O_i), oxygen vacancy (V_O), and their antisites i.e. O sitting at the Zn regular site or vice versa (O_{Zn} or Zn_O) or hydrogen impurities occurring during the synthesis [34]. ZnO exhibit polar and non-polar crystal faces, as described before, due to the anisotropy character of the wurtzite crystal structure [34]. Each crystal face has its individual defect structure leading to the difference in the electronic and optical properties [34]. The interaction of thermal phonons with the defect of each crystal face is dependent on the crystal face [34]. This dependence leads to the introduction of new energy levels in ZnO and give the reason of the obtained red shift in the energy gap of ZnO.

For Cd doped samples, all the absorption curves show a shift toward higher wavelength as given in Fig. 10b. The optical band gap energy values are (2.2, 2.4 and 2.3 eV for $Zn_{0.999}Cd_{0.001}O$, $Zn_{0.99}Cd_{0.01}O$ and $Zn_{0.9}Cd_{0.1}O$, respectively).

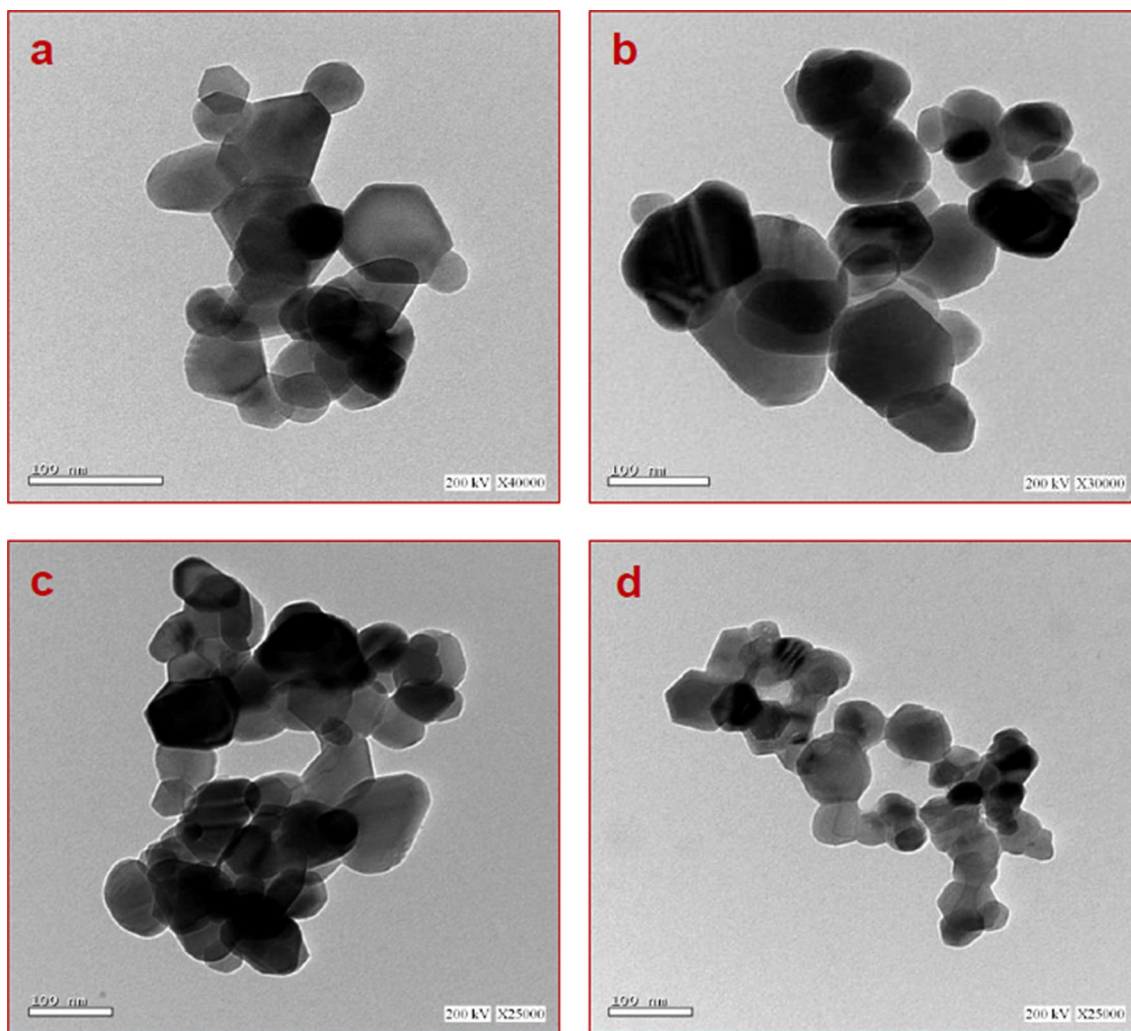


Fig. 9 HRTEM images of different $Zn_{1-x}Cd_xO$ nanoparticles. **a** ZnO, **b** $Zn_{0.999}Cd_{0.001}O$, **c** $Zn_{0.99}Cd_{0.01}O$ and **d** $Zn_{0.9}Cd_{0.1}O$

The sample $Zn_{0.999}Cd_{0.001}O$ shows the highest red shift when compared to the samples $Zn_{0.99}Cd_{0.01}O$ and $Zn_{0.9}Cd_{0.1}O$, Fig. 10b.

It is known that pure CdO is a n-type degenerate semiconductor with a simple cubic structure having a direct band gap of 2.2–2.7 eV and two indirect band gaps of (1.18–1.2) eV and (0.8–1.12) eV with high carrier mobility [35]. Normally its introduction in the wurtzite structure can tune the optical and electronic properties of the studied materials by introducing new energy levels. [30, 36]. The reduction of energy gap can be done by varying the valence band, the conduction band or both [37]. The impact of intrinsic defects on the band structure may vary the band gap position and the Fermi level and so affecting the energy gap value.

When, Cd^{2+} ions substitute Zn^{2+} ions into ZnO lattice, the free electrons in the bottom of the conduction band decrease and the number of vacancies increases, which alter the Fermi level to a lower position of conduction band.

Thus, the excitation energy necessary for electrons transition from valence band to the Fermi level in the conduction band decreases [38].

Also we can deduce that by introducing Cd to ZnO a decrease in the band gap was observed. Both ions have the same outer electronic structure but the core structure of these ions is different. The difference in the core structure leads to the formation of electron trap levels (exciton levels) [14]. The exciton levels are formed just below the conduction band and give a narrower energy band gap [14].

These different factors, explaining the red shift occurrence, are added to both extrinsic and intrinsic factors discussed above in pure ZnO and resulted in the given red shift observed in the energy gap values. The variation of energy gap values with the amount of Cd added is given in Fig. 10c.

As mentioned in the introduction section the particle size and energy gap values differ according to the preparation methods. Table 3 show a comparison of the achieved

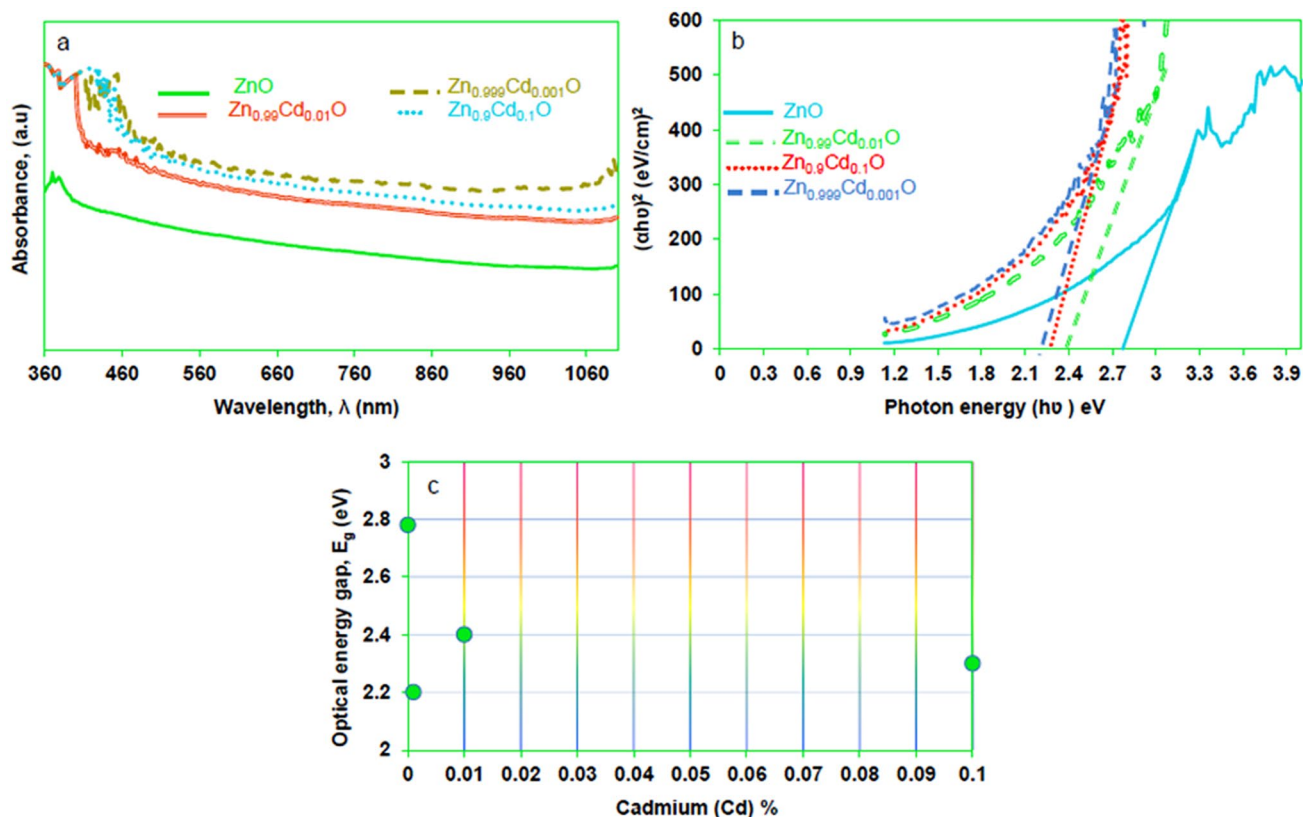


Fig. 10 **a** UV-vis absorption spectra of different $Zn_{1-x}Cd_xO$ nanoparticles. **b** Plot of $(\alpha h\nu)^2$ versus $h\nu$ for ZnO and $Zn_{1-x}Cd_xO$ respectively. **c** Variation of the optical energy gap with the amount of Cd added

Table 3 Comparison on the particle size and energy gap values on $Zn_{1-x}Cd_xO$ and $Zn_{1-x}Cu_xO$ prepared using different methods

Material	Method of preparation	x	Thermal temperature	Particle size (nm)	Energy gap values (eV)	Reference
$Zn_{1-x}Cd_xO$	Polyol method	$x=(0, 0.001, 0.01, 0.1)$	500 °C/4 h	28–111	2.2–2.75	Present work
$Zn_{1-x}Cd_xO$	Auto-combustion	$x=(0, 1, 3, 5)$	500 °C/2 h	30–40	3.2–3.246	[39]
$Zn_{1-x}Cd_xO$	Co-precipitation	$x=(0, 0.03, 0.07)$	1000 °C	28.2–34.5	2.5–3.1	[40]
$Zn_{1-x}Cd_xO$	Sonochemical method	$x=(0, 0.15, 0.3, 0.6, 1)$	–	2.5–5	3.375–3.508	[41]
$Zn_{1-x}Cu_xO$	Solid state reaction	$x=(0, 0.02)$	600 °C/8 h	33–45	3.08–3.25	[42]

The ranges of particle size and energy gap values are independent on the order of x values

particle size and energy gap of $Zn_{1-x}Cd_xO$ (in the present work and other references) and $Zn_{1-x}Cu_xO$ according to the used preparation method. The thermal temperature for giving the studied phase differs according to the used method. The lowest thermal temperature is given in our work and [39]. Other methods need a high temperature and/or a high time of processing. Despite that we have higher values in particle size when compared to the other samples; we have the lowest energy gap values in pure and doped samples. This result confirms the preparation of very high deficient materials having a wide response in the visible region with respect to the other references. As concluded the type and the amount of defects can be

tailored according to the preparation conditions as mentioned before.

3.6 Vibrating Sample Magnetometry Measurements (VSM)

Vibrating sample magnetometry (VSM) technique was used for the magnetic characterization of the synthesized $Zn_{1-x}Cd_xO$ nanoparticles. As shown in Fig. 11a, b except for $x=0.01$, diamagnetic behavior was identified for the undoped and doped ZnO nanoparticles. For $x=0.01$, both ferromagnetic and diamagnetic character were observed. In this case, the coercivity $H_c(0.01)=64.6$ G. Figure 11c

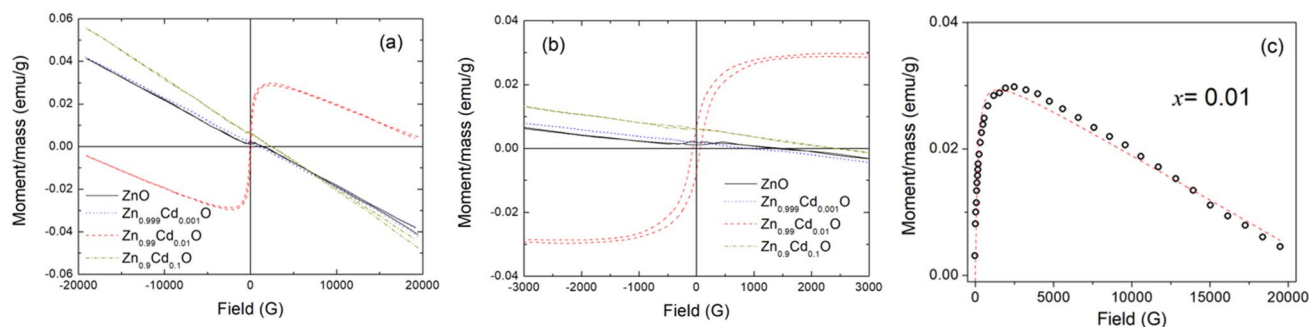


Fig. 11 **a** Hysteresis loops of $Zn_{1-x}Cd_xO$ samples at room temperature. **b** Magnified hysteresis loops showing ferromagnetic behavior for $x=0.01$. **c** Fitting according to the BMP model for $Zn_{0.99}Cd_{0.01}O$ nanoparticles

Table 4 The fitting parameters of bound magnetic polarons model for $Zn_{0.99}Cd_{0.01}O$ nanoparticles

$x=0.01$	
N	7.3935E20
m_s	4.5345E-23
X_m	-1.4293E-6
H_c	64.564 G

illustrates the fitting of $M(H)$ curve of $x=0.01$ using the bound magnetic polarons model [43, 44]. The fitting parameters of bound magnetic polarons model are listed in Table 4. The number of bound magnetic polarons is almost 7×10^{20} , whereas the diamagnetic contribution is amount to $X_m = -1.43 \times 10^{-6}$.

3.7 Electron Spin Resonance Measurements (ESR)

ESR spectroscopy is used to investigate the presence of the unpaired electrons in any material. Accordingly, it is possible to characterize the magnetic properties developed from the surface defects, impurity atoms or dopants, radicals; organic or inorganic, oxygen vacancies etc. Although, pure ZnO possesses non-magnetic behavior, however, ESR peaks can be observed due to the presence of intrinsic defects which are zinc and oxygen vacancies/interstitials and some are extrinsic created by doping as expected before from UV-vis study. ZnO nanostructures have three different charge states of oxygen vacancies; V_0^+ , V_0^{2+} and neutral oxygen vacancies (V_0^x) [45, 46]. Only singly ionized oxygen vacancies V_0^+ has paramagnetic nature and can be responsible for ESR signal. The g-factor can be calculated from the resonance field as [18]:

$$g = \frac{h\nu}{\mu_B H_{res}} \quad (8)$$

where h is the Planck constant, ν is the applied microwave frequency (9.71 GHz), μ_B is the Bohr magneton and H_{res} is the resonance magnetic field. The ESR spectra of

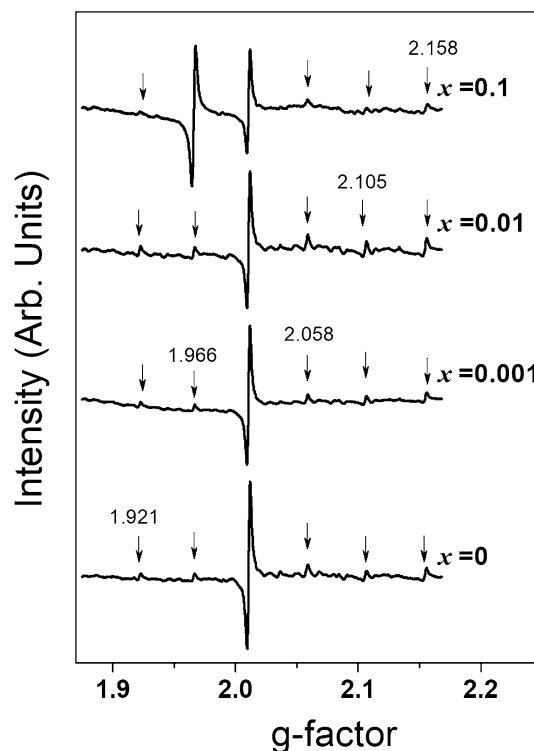


Fig. 12 ESR spectra of $Zn_{1-x}Cd_xO$ nanoparticles at room temperature, the g-factor values of the different lines are indicated

different $Zn_{1-x}Cd_xO$ nanoparticles are shown in Figs. 12 and 13. For all the samples the ESR response is characterized with a strong signal near to the g-factor 2.01. In addition to this strong pronounced signal, five satellite signals were observed as presented in Fig. 12. Only for $x=0.1$, the signal at $g=1.966$ is significantly clear and has more intensity than the signal at $g=2.01$. By fitting the ESR spectra (Fig. 13), the ESR parameters of the main signals were determined and shown in Fig. 14. The g-factor of the main line is amount to 2.01016 for pure ZnO and then decreased with the initial introduction of Cd^{2+} ions to the unit cell ($g(x=0.001)=2.00979$), later the g-factor increased for higher

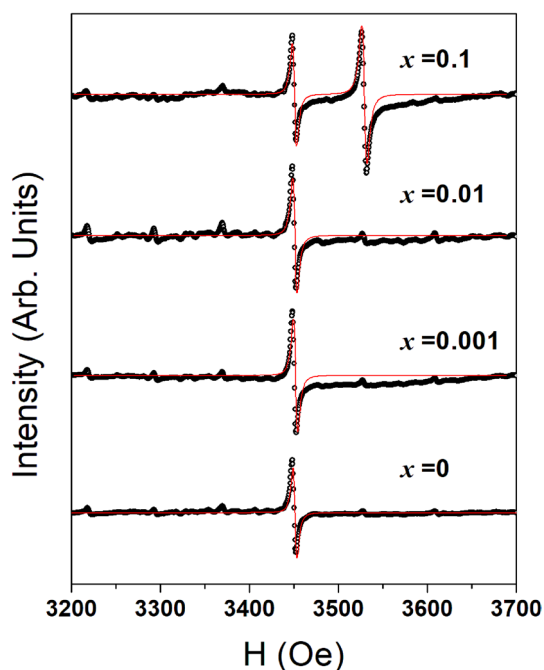


Fig. 13 ESR spectra of $\text{Zn}_{1-x}\text{Cd}_x\text{O}$ nanoparticles at room temperature. Red line represents Lorentzian fitting

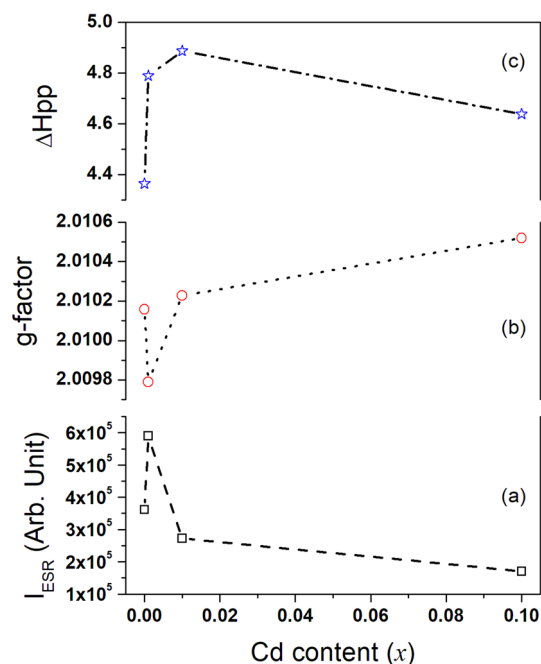


Fig. 14 **a** ESR intensity, **b** g-factor, **c** ESR linewidth (ΔH_{pp}) of different $\text{Zn}_{1-x}\text{Cd}_x\text{O}$ nanoparticles.

Cd content, $g = 2.01023$ and 2.01052 for $x = 0.01$ and 0.1 , respectively. For these ESR lines, the linewidth is ranging between 4.36 Oe and 4.89 Oe, whereas, it reaches its maximum for $x = 0.01$. The intensity of the main ESR line

is initially increased for $x = 0.001$ and then decreased for the higher x values. ESR lines with g -factor 2.01016 , 2.058 and 2.158 can be associated with the chemisorbed oxygen molecules in ZnO surface or the extrinsic properties leading to phonon production. The values of the g -factor of these lines are very close to the free electron g -factor ($g = 2.0023$) which suggest weak orbital magnetic moment [20]. On the other hand, ESR lines with g -factor 1.966 and 1.921 can be associated with the intrinsic singly ionized oxygen vacancies in ZnO structures. For $x = 0.1$, the line at $g = 1.966$ has a linewidth 5.8 Oe.

4 Conclusion

$\text{Zn}_{1-x}\text{Cd}_x\text{O}$ ($x = 0, 0.001, 0.01, 0.1$) nanoparticles were successfully synthesized using polyol technique. X-ray powder diffraction confirmed the formation of single hexagonal wurtzite phase for all the prepared samples. The average particle size of all the samples except for $x = 0.001$ are lower than 80 nm. High resolution transmission electron microscope images support XRD measurements and confirm that $\text{Zn}_{0.999}\text{Cd}_{0.001}\text{O}$ has the largest D . Fourier transformed infrared spectroscopy spots a gradual shift of Zn–O vibration mode by increasing Cd^{2+} content. Scanning electron microscope images show a uniform distribution of the nanoparticles; this may suggest that Cd^{2+} ions have a minor effect on ZnO microstructure. Ultraviolet visible spectroscopy measurements suggest marked red shift in the energy gap values in comparison to the theoretical values. The band gap energy is maximum for ZnO nanoparticles and decreases for Cd^{2+} ions doped samples. Only for $\text{Zn}_{0.99}\text{Cd}_{0.01}\text{O}$, $M(H)$ curve spots ferromagnetic behavior which can be well described by bound magnetic polarons model. For the remaining samples, diamagnetic behavior was observed. Electron spin resonance measurements showed the signature of O and Zn vacancies. The ESR spectra of all the samples show the signature of the presence of crystal imperfections like defects which are either extrinsic, intrinsic defects or chemisorbed oxygen molecules.

References

1. Q. Wang, Y. Yan, Y. Zeng, Y. Lu, L. Chen, Y. Jiang, Free-standing undoped ZnO microtubes with rich and stable shallow acceptors. *Sci. Rep.* **6**, 27341 (2016). <https://doi.org/10.1038/srep27341>
2. B. Hussain, A. Aslam, T.M. Khan, M. Creighton, B. Zohuri, Electron affinity and bandgap optimization of zinc oxide for improved performance of ZnO/Si heterojunction solar cell using PC1D simulations. *Electronics* **8**, 238 (2019). <https://doi.org/10.3390/electronics8020238>
3. J. Luo, K. Zhang, M. Cheng, M. Gu, X. Sun, MoS_2 spheres decorated on hollow porous ZnO microspheres with strong

- wideband microwave absorption. *Chem. Eng. J.* **380**, 122625 (2020). <https://doi.org/10.1016/j.cej.2019.122625>
4. A. Kołodziejczak-Radzimska, T. Jesionowski, Zinc oxide: from synthesis to application: a review. *Materials* **7**, 2833–2881 (2014)
 5. G. Ogibene, D.A. Cristaldi, R. Fiorenza, I. Blanco, G. Cicala, S. Scirè, Photoactivity of hierarchically nanostructured ZnO PES fibre mats for water treatments. *RSC Adv.* **6**, 42778–42785 (2016)
 6. A.R. Prasad, S.M. Basheer, I.R. Gupta, K.K. Elyas, A. Joseph, Investigation on Bovine Serum Albumin (BSA) binding efficiency and antibacterial activity of ZnO nanoparticles. *Mater. Chem. Phys.* **240**, 122115 (2020)
 7. D. Zhang, F. Zeng, Visible light-activated cadmium-doped ZnO nanostructured photocatalyst for the treatment of methylene blue dye. *J. Mater. Sci.* **47**, 2155–2161 (2012)
 8. O. Aguilar, S. De. Castro, M.P.F. Godoy, M.R.S. Dias, Optoelectronic characterization of $Zn_{1-x}Cd_xO$ thin films as an alternative to photonic crystals in organic solar cells. *Opt. Mater. Express.* **9**, 3638 (2019). <https://doi.org/10.1364/OME.9.003638>
 9. A. Janotti, C.G. van Walle, Fundamentals of zinc oxide as a semiconductor. *Rep. Prog. Phys.* **72**, 126501 (2009)
 10. T.A. Geleta, T. Imae, Influence of additives on zinc oxide-based dye sensitized solar cells. *Bull. Chem. Soc. Jpn.* **93**, 611–620 (2020). <https://doi.org/10.1246/bscj.20200001>
 11. Y. Wang, Y. Yang, X. Zhang, X. Liu, A. Nakamura, Optical investigation on cadmium-doped zinc oxide nanoparticles synthesized by using a sonochemical method. *Cryst. Eng. Commun.* **14**, 240–245 (2012)
 12. S. Kurajica, V. Mandić, G. Matijašić, I.K. Munda, K. Mužina, Mechanochemical synthesis of zincite doped with cadmium in various amounts. *Sci. Eng. Compos. Mater.* **26**, 482–490 (2019)
 13. L. Arda, M. Açıkgöz, A. Güngör, Magnetic and microstructure properties of Ni-doped ZnO films and powder by sol-gel process. *J. Supercond. Nov. Magn.* **25**, 2701–2705 (2012)
 14. A. Morais, R.A. Torquato, U.C. Silva, C. Salvador, C. Chesman, Effect of doping and sintering in structure and magnetic properties of the diluted magnetic semiconductor ZnO:Ni. *Cerâmica* **64**, 627–631 (2018). <https://doi.org/10.1590/0366-69132018643722463>
 15. N. Ali, A.R. Vijaya, Z.A. Khan, K. Tarafder, A. Kumar, M.K. Wadhwa, B. Singh, S. Ghosh, Ferromagnetism from nonmagnetic ions: Ag-doped ZnO. *Sci. Rep.* **9**, 20039 (2019). <https://doi.org/10.1038/s41598-019-56568-8>
 16. A. Guler, L. Arda, N. Dogan, C. Boyraz, E. Ozugurlu, The annealing effect on microstructure and ESR properties of (Cu/Ni) codoped ZnO nanoparticles. *Ceram. Int.* **45**, 1737–1745 (2019)
 17. S.P. Bharath, K.V. Banger, G.K. Shivakumar, Effect of cadmium incorporation on the properties of zinc oxide thin Films. *Appl. Nanosci.* **8**, 187–193 (2018)
 18. M. Yehia, Sh. Labib, S.M. Ismail, Structural, optical, and magnetic properties of Co-doped SnO₂ nanoparticles. *J. Electron. Mater.* **48**, 4170–4178 (2019)
 19. M. Bortolotti, L. Lutterotti, I. Lonardelli, ReX: a computer program for structural analysis using powder diffraction data. *J. Appl. Cryst.* **42**, 538–539 (2009)
 20. H. Morkoç, Ü. Özgür, *Zinc Oxide: Fundamentals, Materials and Device Technology* (Wiley-VCH Verlag GmbH & Co, KGaA, 2009)
 21. J.A. Dean, *Lange's Handbook of Chemistry* (McGraw-Hill, New York, 1999)
 22. D.D. Thongam, J. Gupta, N.K. Sahu, Effect of induced defects on the properties of ZnO nanocrystals: surfactant role and spectroscopic analysis. *SN Appl. Sci.* **1**, 1030 (2019)
 23. A.B.D. Nandiyanto, R. Oktiani, R. Ragadhita, How to read and interpret FTIR spectroscopy of organic material. *IJOST* **4**, 97–118 (2019)
 24. M.D. Bohon, B.A. Metzger, W.P. Linak, C.J. King, W.L. Roberts, Glycerol combustion and emissions. *Proc. Symp. Combust.* **33**, 2717–2724 (2011)
 25. M.K. Ahmed, M.P. McLeod, J. Nézar, A.W. Giuliani, Fourier transform infrared and near-infrared spectroscopic methods for the detection of toxic diethylene glycol (DEG) contaminant in glycerin based cough syrup. *Spectroscopy* **24**, 601–608 (2010)
 26. K.S. Babu, A.R. Reddy, C. Sujatha, K.V. Reddy, A.N. Mallika, Synthesis and optical characterization of porous ZnO. *J. Adv. Ceram.* **2**, 260–265 (2013)
 27. L.P. Etcheverry, W.H. Flores, D.L. da Silva, E.C. Moreira, Annealing effects on the structural and optical properties of ZnO nanostructures. *Mater. Res.* **21**(e20170936), 1–7 (2018)
 28. H. Gupta, J. Singh, R.N. Dutt, S. Ojha, S. Kar, R. Kumar, V.R. Reddy, F. Singh, Defect-induced photoluminescence from gallium-doped zinc oxide thin films: influence of doping and energetic ion irradiation. *Phys. Chem. Chem. Phys.* **21**, 15019–15029 (2019)
 29. J. Singh, P. Kumar, K.N. Hui, J. Jung, R.S. Tiwari, O.N. Srivastava, Morphological evolution, structural and optical investigations of ZnO: Mg ($Mg_xZn_{1-x}O$ ($0 \leq x \leq 30\%$)) nanostructures. *RSC Adv.* **3**, 5465–5474 (2013)
 30. Sh. Labib, Preparation, characterization and photocatalytic properties of doped and undoped Bi₂O₃. *J. Saudi Chem. Soc.* **21**, 664–672 (2017)
 31. N. Kamarulzaman, M.F. Kasim, R. Rusdi, Band gap narrowing and widening of ZnO nanostructures and doped materials. *Nanoscale Res. Lett.* (2015). <https://doi.org/10.1186/s11671-015-1034-9>
 32. M. Maldoan, Phonon wave interference and thermal bandgap materials. *Nat. Mater.* **14**, 667–674 (2015)
 33. X. Wu, J. Lee, V. Varshney, J.L. Wohlwend, A.K. Roy, T. Luo, Thermal conductivity of wurtzite zinc-oxide from first-principles lattice dynamics—a comparative study with gallium nitride. *Sci. Rep.* (2016). <https://doi.org/10.1038/srep22504>
 34. K. Saravanan, R. Krishnan, S.H. Hsieh, H.T. Wang, Y.F. Wang, W.F. Pong, K. Asokan, D.K. Avasthi, D. Kanjilal, Effect of defects and film thickness on the optical properties of ZnO–Au hybrid films. *RSC Adv.* **5**, 40813–40819 (2015)
 35. Q.A.H. Al-Naser, J. Zhou, G. Liu, L. Wang, Zn_{1-x}Cd_xO Microtubes: synthesis and optical properties using direct microwave irradiation. *High Temp. Mater. Proc.* **36**, 921–926 (2017)
 36. S. Labib, Study of photocatalytic properties of pure and doped ZnO powders. *Mat.-wiss. u. Werkstofftech.* **47**, 19–28 (2016)
 37. I.J.T. Jensen, K.M. Johansen, W. Zhan, V. Venkatachalapathy, L. Brillson, A.Yu. Kuznetsov, Ø. Prytz, Bandgap and band edge positions in compositionally graded ZnCdO. *J. Appl. Phys.* **124**(015302), 1–8 (2018)
 38. B.J. Zheng, J.S. Lian, L. Zhao, Q. Jiang, Structural, optical and electrical properties of Zn_{1-x}Cd_xO thin films prepared by PLD. *Appl. Sur. Sci.* **257**, 5657–5662 (2011)
 39. R. Liu, D. Zhao, L. Duan, X. Zhao, Optical and photocatalytic properties of Zn_{1-x}Cd_xO nanoparticles with tuned oxygen vacancy. *J. Alloys Compd.* **825**, 153377 (2020). <https://doi.org/10.1016/j.jallcom.2019.153377>
 40. P. Bhardwaj, M.F. Ansari, J. Singh, R. Kumar, V. Verma, A study of structural and optical properties of Cd doped zinc oxide (Zn_{1-x}Cd_xO) nanoparticles prepared by co-precipitation method. *AIP Conf. Proc.* **2265**, 030125 (2019). <https://doi.org/10.1063/1.50016591>
 41. H.-X. Zhang, Y.-T. Yang, X.-J. Liu, Study of cadmium-doped zinc oxide nanocrystals with composition and size dependent band gaps. *Chin. J. Chem. Phys.* **31**, 197–202 (2018). <https://doi.org/10.1063/1674-0068/31/cjcp1708181>
 42. R. Elilarassi, G. Chandrasekaran, Structural, optical and magnetic characterization of Cu-doped ZnO nanoparticles synthesized

- using solid state reaction method. *J. Mater. Sci.* **21**, 1168–1173 (2010). <https://doi.org/10.1007/s10854-009-0041-y>
43. T. Debnath, S. Das, D. Das, S. Sutradhar, Optical, magnetic, and dielectric properties of ZnO: Y nanoparticle synthesized by hydrothermal method. *J. Alloys Compd.* **696**, 670–681 (2017)
 44. A. Bandyopadhyay, S. Sutradhar, B.J. Sarkar, A.K. Deb, P.K. Chakrabarti, Vacancy mediated room temperature ferromagnetism in Co-doped Dy₂O₃. *Appl. Phys. Lett.* **100**, 252411 (2012)
 45. A.L. Taylor, G. Filipovich, G.K. Lindeberg, Electron paramagnetic resonance associated with Zn vacancies in neutron-irradiated ZnO. *Solid State Commun.* **8**, 1359–1361 (1970)
 46. D. Galland, A. Herve, ESR spectra of the zinc vacancy in ZnO. *Phys. Lett. A* **33**, 1–2 (1970)

Publisher's Note Springer Nature remains neutral with regard to jurisdictional claims in published maps and institutional affiliations.